Research Paper

Journal of Chemical Research

Journal of Chemical Research
2019, Vol. 43(11-12) 531–541

DOI: 10.1177/1747519819875859
journals.sagepub.com/home/chl
SAGE

The synthesis and spectroscopic characterization of (+)-demethoxyaspidospermine: Density functional theory calculations of the structural, electronic, and non-linear optic and spectroscopic properties

Goncagül Serdaroğlu[1] and Nesimi Uludağ[2]

Abstract

(+)-Demethoxyaspidospermine was synthesized via the acylation of aspidospermidine with acetic anhydride, and the structure was determined by elemental analysis and Fourier-transform infrared and nuclear magnetic resonance spectroscopic tools and was supported by the simulated spectroscopic studies. Next, the stable geometries obtained by the conformational analysis performed at the B3LYP/6-31G(d, p) level were used for further investigations carried out in B3LYP and M06-2X functionals, and Hartree–Fock (HF) method, employed by the 6-311++G(d, p) basis set. Also, the natural bond orbital analysis revealed that the most contribution to the lowering of the stabilization energy came from $n \rightarrow \pi^*$ and $\pi \rightarrow \pi^*$ interactions. Moreover, the non-linear optic analysis has shown that the title compound can be a useful agent in the optoelectronic devices because of the optical properties. Also, the chemical reactivity tendency for nucleophilic or electrophilic attack reactions on the compound was evaluated by frontier molecular orbital analysis, and the reactive sites of the compound was shown by highest molecular orbital and lowest unoccupied orbital amplitudes and molecular electrostatic potential diagrams.

Keywords

(+)-demethoxyaspidospermine, donor–acceptor systems, frontier molecular orbital analysis, Fourier-transform infrared, non-linear optic, nuclear magnetic resonance

Date received: 10 June 2019; accepted: 21 August 2019

Introduction

The unique structure of demethoxyaspidospermine and the diverse bioactivities of Aspidosperma alkaloids have long been of interest and have attracted much attention and extensive research by the synthetic community for more than 40 years, which continues to the present day. Aspidosperma-type alkaloids with a pentacyclic framework have been isolated from a range of plant sources, including the stem bark of *Aspidosperma pyrifolium* Mart, which contains the following alkaloids: vincadifformine, vallesine, demethoxyaspidospermine, and aspidospermidine. Aspidosperma species have a long history of medicinal applications, including the treatment of malaria and fever in South American countries.[1–3] The unique molecular architecture and the vast array of important biological activities[4,5] characterizing many of these alkaloids have generated intense research interest over the years.[6,7] Although alkaloids with complex structures that belong to the Aspidosperma family have been the subject of growing interest, investigations of their synthesis have been limited to several alkaloids and related compounds that comprise their basic skeleton.[8–10] The core structure of Aspidosperma alkaloids is typically a pentacyclic **ABCDE** framework, and there are more than 250 of this type. Their unique molecular architectures and pharmacological activities have led to intense investigation of these alkaloids.[11–13] Considering the above, we have developed a new approach for synthesizing demethoxyaspidospermine, whose structure was first synthesized after being isolated and reported in literature. Both the synthesis and framework of this complex structure are critical and must be precisely determined. In the past, there have been reports of the syntheses of both aspidospermidine and strychnos-type alkaloids,[14–17] but the leading role of the intermolecular or

[1]Department of Science Education, Sivas Cumhuriyet University, Sivas, Turkey
[2]Department of Chemistry, Tekirdag Namik Kemal University, Tekirdag, Turkey

Corresponding author:
Goncagül Serdaroğlu, Department of Science Education, Sivas Cumhuriyet University, Sivas 58140, Turkey.
Email: goncagul.serdaroglu@gmail.com

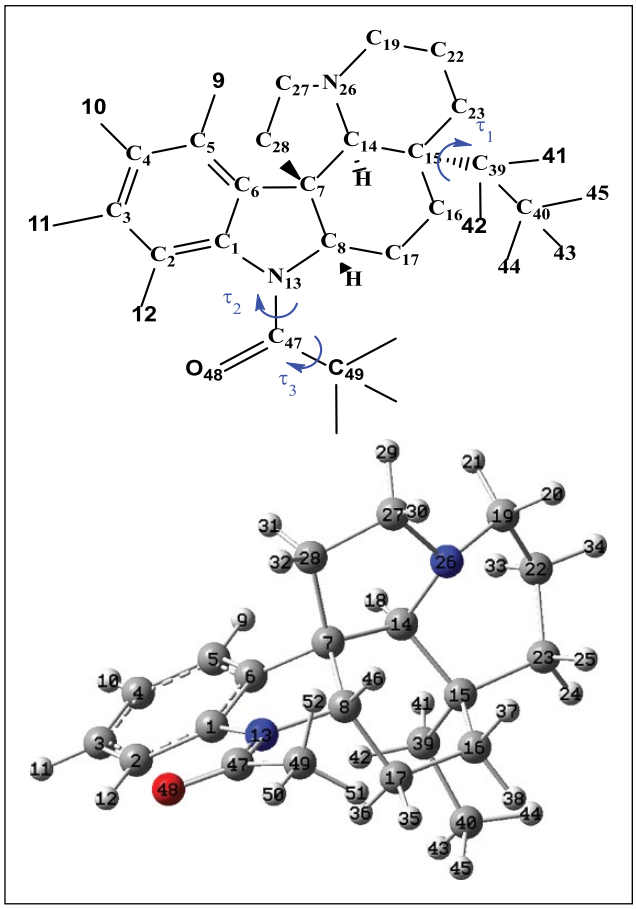

Figure 1. The chemical structure with the dihedral angles defined as τ_1 (C40–C39–C15–C14), τ_2 (O48–C47–N13–C8), and τ_3 (C49–C47–N13–C8) and optimized structure of demethoxyaspidospermine (given in Scheme 1).

intramolecular interactions on the challenging syntheses of this group of compounds has rarely been reported by using computational tools.[18–20]

For this reason, we decided to investigate the structure, electronic, and spectroscopic properties of demethoxyaspidospermine because the results might provide useful information for synthetic chemists. In this paper, we selected aspidospermidine as our starting material[20,21] and then performed the acylation of compound **1** with acetic anhydride in 81% of the overall yield. Recently, we determined the structure of synthetic demethoxyaspidospermine by nuclear magnetic resonance (NMR), Fourier-transform infrared (FTIR), and elemental analysis. Following the structural investigation of the demethoxyaspidospermine by the potential energy surface (PES) analysis, we have performed NMR and FTIR spectroscopic analyses for all stable structures and compared the recorded ^{1}H and ^{13}C NMR shifts of the title compound with the calculated values. Next, the electronic and optical properties of the title compound were investigated by natural bond orbital (NBO) and non-linear optic (NLO) analyses. Consequently, the chemical reactivity tendency and reactive sites of demethoxyaspidospermine have been clarified by frontier molecular orbital (FMO) analyses and molecular electrostatic potential (MEP) diagrams.

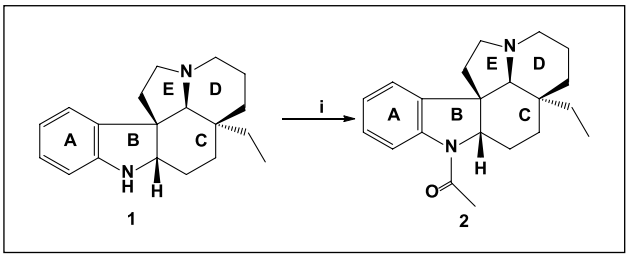

Scheme 1. The synthesis of (+)-demethoxyaspidospermine.
i: tetrabutylammonium hydrogensulfate (97%), sodium hydroxide, acetic anhydride, CH_2Cl_2 (81%), 0 °C for 2 h and then room temperature for 6 h.

Results and discussion

Conformational analysis and molecular geometry

The conformational analysis of the title compound illustrated in Figure 1 has been performed with the dihedral angles that are τ_1 (C40–C39–C15–C14), τ_2 (O48–C47–N13–C8), and τ_3 (C49–C47–N13–C8) changing in steps of 10° from 0° to 360°. The conformational analysis curves for the dihedral angles τ_1 and τ_2 are given in Figure 2 because the stable conformers obtained from the dihedral angles τ_2 and τ_3 according to rotation of the acetyl group around the rings A, B, and C (RA, RB, and RC) are found to be similar to each other. Also, the total and relative energies as a function of each torsion angle during the PES scan of demethoxyaspidospermine are given in Supplemental Table S1 (see the Supporting Information).

From Figure 2, the five stable conformers have been determined by the PES analysis according to the acetyl and ethyl group orientation around the ring system of the title compound. These stable conformers have been re-optimized by the M06-2X level, B3LYP level, and HF method of the 6-311++G(d, p) basis set. According to Supplemental Table S1, the relative energies of five stable conformers have been determined in the chloroform phase as 0.0 and 3.34 kcal mol^{-1} by the B3LYP level, 0.0–3.84 kcal mol^{-1} by the M06-2X level, and 0.0–4.39 kcal mol^{-1} by the HF method. From Supplemental Table S1, **CI** has been identified as the lowest energy conformer by the B3LYP level, but for the HF method and M06-2X level of the density functional theory (DFT) method, **CIV** has been calculated as the most stable structure.

Table 1 shows the optimized geometric parameters of the five stable conformers for demethoxyaspidospermine; full data have been given in Supplemental Table S2. We have compared selected parameters for the title compound with structurally related indole derivatives[22,23] because of no experimental and computational data. It is clear that the bond lengths are very similar to each other. As expected, the aromatic C–C bond lengths for **CI** has been simulated in the range 1.39–1.40 Å, while the non-aromatic C–C bond lengths for **CI** have been predicted in the range 1.52–1.57 Å. In the past, the aromatic and non-aromatic bond lengths for 2-(2,2-Dimethoxyethyl)-3-oxo-1,2,3,4,5,6-hexahydro-1,5-methano-7*H*-azocino[4,3-*b*]indole were observed in the range of 1.37–1.41 Å and 1.52–1.57 Å, respectively.[22] Also, we have predicted the N13–C1 and

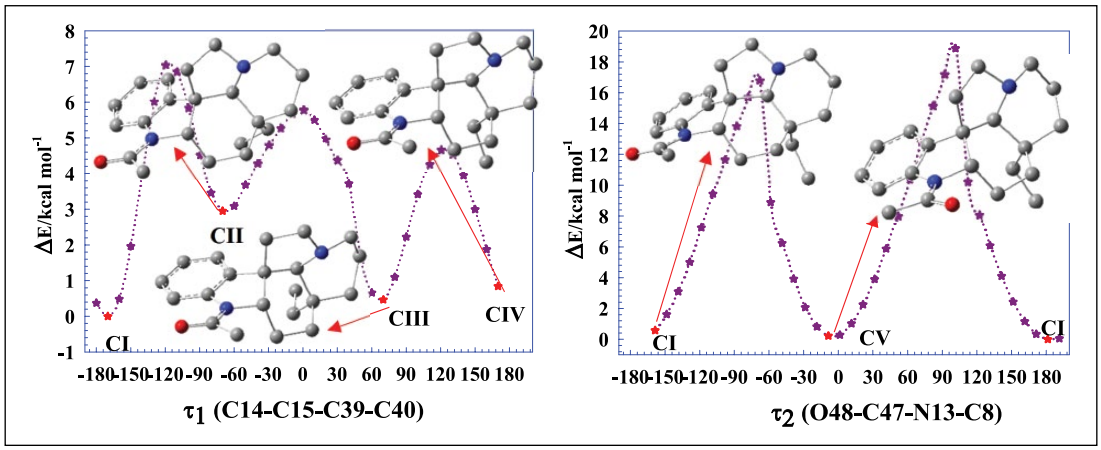

Figure 2. The PES curves and stable conformers of demethoxyaspidospermine at the B3LYP/6-31G(d, p) level in the gas phase.

N13–C8 bond lengths as 1.42 and 1.49 Å, respectively, while both bond lengths were determined as 1.38 Å.[22] As expected, the C=O bond length for each conformer has been calculated as 1.23 Å for the B3LYP level, while it has been found to be 1.21 Å for the HF method. As expected, the C–C–C bond angles for the aromatic R**A** have been simulated as C2–C1–C6 = 121.5°, C1–C2–C3 = 117.95°, C2–C3–C4 = 121.17°, C3–C4–C5 = 120.15°, C4–C5–C6 = 119.48°, and C5–C6–C1 = 119.75° for **CI** with B3LY. In the past, the same bond angles were observed as 122.4°, 117.60°, 121.20°, 121.7°, 118.90°, and 118.18°.[22] In addition, the C–C–C angles for the non-aromatic R**C** and R**D** for **CI** have been calculated as C14–C15–C16 = 110.75°, C15–C16–C17 = 112.74°, and C15–C23–C22 = 112.56° by the B3LYP level, whereas these bond angles have been observed as 108.2°, 113.30°, and 119.29°.[22,23]

Also, it is worth discussing the dihedral angles of all conformers. It should be noted that the C40–C39–C15–C14 dihedral angle for **CI**, **CII**, **CIII**, **CIV**, and **CV** are at −170.95°, −67.68°, 67.53°, −171.71°, and −171.29° for the B3LYP level and at −169.75°, −69.43°, 67.54°, −170.50°, and −169.82° for the HF method, respectively. It is clear that the ethyl group for each of **CI**, **CIV**, and **CV** conformers has deviated from the C40–C39–C15–C14 backbone by −8° around, while the ethyl group for other conformers (**CII** and **CIII**) has deviated by −112° around. Although **CI**, **CII**, and **CV** have exhibited the same deviation in terms of the ethyl group, **CI** and **CV** are almost mirror images of each other according to the orientation of the acetyl group. The C27–C28···C8 angles for **CIII** and **CIV** have been estimated at 103.52° and 104.20°, respectively, while this angle for **CI**, **CII**, and **CV** has been determined at 125.98°, 128.04°, and 125.99°, respectively, with the B3LYP level. As can be seen from the other non-bonding angles that are C27–C28···C17, C27–C28···C16, and C27–N26···C16, the R**E** for **CIII** and **CIV** has folded over the R**C** more than that of other conformers.

NBO analysis

NBO analysis using the second-order perturbative theory results provide the useful information of the hybridization and covalency effects in the polyatomic wave function as a chemical phenomenon being important in terms of the prediction of the intramolecular and intermolecular interactions such as the intramolecular charge transfer, H-bonding tendency, and conjugative interactions.[24,25] Weinhold et al.[24,25] have defined the second-order perturbative energy lowering for a specific molecular system due to the electron delocalization or electron density transfer from the filled bonding orbital (or lone pairs) of the "Lewis base" into the unfilled antibonding orbital "Lewis acid." The stabilization energy $(E^{(2)} = \Delta E_{ij} = qi((Fij)^2 / (\varepsilon j - \varepsilon i)))$ for a specific donor $(i) \rightarrow$ acceptor (j) interaction depends on the donor orbital occupancy (qi), the filled and unfilled orbital energies (εi and εj), and the off-diagonal NBO Fock matrix element (Fij).

The important intramolecular interactions contributing to the lowering of the molecular stabilization energy for each of the stable conformers are given in Supplemental Table S3. We have calculated that the strong electron delocalization from the donor π (C1–C2) orbital to the acceptor π* (C3–C4) and π* (C5–C6) orbitals has been predicted for each stable conformer as follows: 20.71 and 19.06 kcal mol^{-1} (ED_i = 1.65012e) for **CI**, 20.67 and 19.06 kcal mol^{-1} (ED_i = 1.65068e) for **CII**, 21.22 and 20.45 kcal mol^{-1} (ED_i = 1.64715e) for **CIII**, and 20.86 and 19 kcal mol^{-1} (ED_i = 1.66014e) for **CV**. It should be noted from Supplemental Table S3 that the electron delocalization occurred in the aromatic part of each stable conformer is like each other in terms of the second-order perturbative energy lowering. Furthermore, the hyperconjugative interaction energy (σ → π*) for the electron delocalization between σ (C7–C28) and π* (C5–C6) has been determined as 3.37 kcal mol^{-1} for **CI**, 3.52 kcal mol^{-1} for **CII**, 3.68 kcal mol^{-1} for **CIV**, and 3.25 kcal mol^{-1} for **CV**, but this kind of interaction has not been calculated for **CIII**. Also, the resonance energy for the LP(1) N13 → π* (C1–C2) interaction has been predicted as 32.86 kcal mol^{-1} for **CI**, 33.05 kcal mol^{-1} for **CII**, 33.11 kcal mol^{-1} for **CIII**, 32.54 kcal mol^{-1} for **CIV**, and 33.92 kcal mol^{-1} for **CV**. However, it should be noted from Supplemental Table S3 that the strong LP(1) N13 → π* (C47–O48) interaction has been estimated as 55.27 kcal mol^{-1} (ED_i = 1.63806e) for **CII** and 52.79 kcal mol^{-1} (ED_i = 1.63427e) for **CV**. Here, it should also be noted that the LP(1) N13 → π* (C47–O48) interaction has

Table 1. Selected optimized parameters of the demethoxyaspidospermine in the chloroform phase.

	B3LYP/6-311++G(d, p)					
	Exp.	**CI**	**CII**	**CIII**	**CIV**	**CV**
Bond length (Å)						
C1–C2	1.39[a]	1.39	1.39	1.39	1.39	1.39
C1–C6	1.41[a]	1.40	1.40	1.40	1.40	1.41
C1–N13	1.38[a]	1.42	1.42	1.42	1.42	1.42
C5–C6	1.40[a]	1.39	1.39	1.39	1.39	1.39
C6–C7	1.44[a]	1.52	1.52	1.52	1.52	1.52
C7–C14	1.50[a]	1.57	1.57	1.55	1.55	1.57
C14–N26		1.47	1.47	1.47	1.47	1.47
N26–C27		1.46	1.45	1.47	1.47	1.46
C47–O48		1.23	1.23	1.23	1.23	1.23
Bond angle (°)						
C2–C1–C6	122.4[a]	121.5	121.5	121.4	121.4	120.9
C2–C1–N13	130.8[b]	129.2	129.3	129.3	129.3	130.0
C1–C2–C3	117.6[a]	118.0	117.9	117.9	117.9	118.5
C2–C3–C4	121.2[a]	121.2	121.2	121.3	121.3	121.0
C3–C4–C5	121.7[a]	120.2	120.1	120.1	120.1	120.0
C4–C5–C6	118.9[a]	119.5	119.5	119.4	119.4	119.7
C1–N13–C8	108.9[a]	108.4	108.1	108.0	108.0	108.5
C15–C16–C17	113.3[b]	112.7	115.3	113.9	113.4	112.8
C15–C23–C22	119.3[a]	112.6	114.0	113.4	112.9	112.6
Non-bonding angle (°)						
C27–C28···C8		126.0	128.0	103.5	104.2	126.0
C27–C28···C17		112.2	114.4	96.0	96.6	112.1
C27–C28···C16		91.0	94.3	77.3	77.5	90.9
C27–N26···C16		130.4	129.5	126.8	125.8	130.4
Dihedral angle (°)						
C6–C1–C2–C3	0.70[a]	0.3	0.2	0.3	0.3	−2.0
N13–C1–C6–C5	179.8[b]	179.8	179.9	179.8	179.7	179.6
C4–C5–C6–C1	−0.20[a]	−0.3	−0.4	−0.8	−0.7	−0.9
C6–C7–C14–N26		137.9	132.4	156.4	154.6	137.7
C8–C7–C14–N26		−104.0	−109.4	−83.9	−85.9	−104.2
C28–C7–C14–C15		142.1	137.7	156.4	155.5	141.8
C14–C7–C28–C27		7.7	13.7	−31.4	−30.6	7.7
C16–C15–C23–C22		−153.9	−166.9	−137.5	−140.0	−153.1
C39–C15–C23–C22		83.8	73.8	103.1	96.5	84.5
C14–C15–C39–C40		−171.0	−67.7	67.5	−171.7	−171.3

Source: Available experimental data are taken from [a]Hökelek et al.[22] and [b]Murugavel et al.[23]

not been calculated for **CI**, **CIII**, and **CIV**. The strongest hyperconjugative interaction for **CII** has been determined as $E^{(2)}=19.10\,\text{kcal mol}^{-1}$ ($ED_i=1.97254$e) for the σ (C49–H52)→π* (C47–O48) interaction. From Supplemental Table S3, the other hyperconjugative interactions for **CII** have been determined as σ (C7–C14)→π* (C5–C6) with $E^{(2)}=0.66\,\text{kcal mol}^{-1}$ ($ED_i=1.96779$e), σ (C47–C49)→π* (C47–O48) with $E^{(2)}=1.59\,\text{kcal mol}^{-1}$ ($ED_i=1.98435$e), σ (C49–H50)→π* (C47–O48) with $E^{(2)}=1.17\,\text{kcal mol}^{-1}$ ($ED_i=1.98726$e), and σ (C49–H52)→π* (C47–O48) with $E^{(2)}=19.10\,\text{kcal mol}^{-1}$ ($ED_i=1.97254$e).

NLO properties

The organic aromatic compounds having strong intramolecular charge transfer or electron density transfer between the donor and acceptor couple have been commonly studied since the invention of lasers in the 1960s because they can serve as optical materials used in electro-optic modulation, optical memory, telecommunications, and optical interconnections.[26]

Table 2 shows the μ, α_0, $\Delta\alpha$, and β tensors for all the methods in the chloroform phase calculated at the B3LYP level; the gas phase values are given in Supplemental Table S4. It is clear that the static dipole moment has changed with the conformational structure as well as the solvent dielectric constant, that is, the μ values of all conformers (B3LYP) have been predicted as 4.437 (**CI**), 4.401 (**CII**), 4.365 (**CIII**), 4.363 (**CIV**), and 3.371 (**CV**) D in vacuum (Supplemental Table S4) and 5.691 (**CI**), 5.680 (**CII**), 5.645 (**CIII**), 5.620 (**CIV**), and 4.656 (**CV**) D in chloroform. Accordingly, **CV** has a lower dipole moment value, while **CI** has the highest, which means that **CI** will prefer the intermolecular interaction rather than intramolecular interactions, or vice versa for **CV**. On the other hand, the mean polarizability (α_0) of each

Table 2. The NLO analysis results for demethoxyaspidospermine in the chloroform phase.

	B3LYP/6-311++G(d, p)				
	CI	**CII**	**CIII**	**CIV**	**CV**
μ (Debye)					
M	5.691	5.680	5.645	5.620	4.565
α. esu ($\times 10^{-24}$)					
α_0	47.004	47.043	47.042	47.058	47.155
$\Delta\alpha$	12.602	13.606	13.995	12.565	12.467
β. esu ($\times 10^{-30}$)					
β_x	4.294	4.311	2.443	3.223	−4.893
β_y	1.771	0.198	3.264	3.999	−4.188
β_z	−3.249	−2.863	−1.345	−1.828	6.670
β	5.669	5.179	4.293	5.451	9.272

NLO: non-linear optic.

stable conformer has been calculated close to each other, that is, we have calculated by the B3LYP level the mean polarizability of all stable conformers as **CI** = 37.531×10^{-24} esu, **CII** = 37.498×10^{-24} esu, **CIII** = 37.513×10^{-24} esu, **CIV** = 37.582×10^{-24} esu, and **CV** = 37.645×10^{-24} esu in the gas phase and **CI** = 47.004×10^{-24} esu, **CII** = 47.043×10^{-24} esu, **CIII** = 47.042×10^{-24} esu, **CIV** = 47.052×10^{-24} esu, and **CV** = 47.155×10^{-24} esu in the chloroform phase. Here, it is hard to suggest the most polarizable or soft conformer according to these results. In this context, it is worth evaluating the first-order hyperpolarizability tensors of each stable conformer. We have determined by the B3LYP level the first-order hyperpolarizability (β) values of the **CI**, **CII**, **CIII**, **CIV**, and **CV** conformers of the title compound as 2.692, 2.207, 2.661, 3.172, and 5.712×10^{-30} esu in the gas phase and as 5.669, 5.179, 4.293, 5.451, and 9.272×10^{-30} esu in the chloroform phase, respectively.

From Table 2 and Supplemental Table S4, it can be seen that the β tensors determined by the B3LYP level are nearly twice as high as those of the HF method, in both phases. Also, the calculated first-order hyperpolarizability (β) for **CV** is approximately twice that of the other conformers, which means that **CV** can more likely be used as an optical material than the other conformers. In the past, the dipole moment and first-order hyperpolarizability for urea were calculated[27] by the same theory level as 1.7676 D and 0.6230×10^{-30} esu, respectively. Based on the β tensors of the title compound, we can suggest that the title compound can be used as a material for optoelectronic devices because the β tensor of each stable conformer of the title compound is remarkably higher than that of the urea.

Chemical reactivity descriptors, FMO analysis, MEP diagrams

The highest molecular orbital (HOMO), the lowest unoccupied orbital (LUMO), and the HOMO–LUMO gap energy ($\Delta E = E_{LUMO} - E_{HOMO}$) have been used to evaluate the kinetic stability and chemical reactivity of a specific molecular system.[28,29]

The calculated quantum chemical parameters computed in the chloroform phase are given in Table 3; all data are provided in Supplemental Table S5. Accordingly, the energy gap ranking has been calculated as follows: **CIII** (4.9658 eV) < **CIV** (4.9707 eV) < **CV** (5.1383 eV) < **CI** (5.2817 eV) < **CII** (5.2994eV) by the B3LYP level and **CII** (7.1974 eV) < **CI** (7.1990 eV) < **CIII** (7.2094 eV) < **CIV** (7.2137 eV) < **CV** (7.2635 eV) by the HF method, in the chloroform phase with the 6-311++G(d, p) basis set. The energy gap value is calculated in different orders depending on the methods (or functionals for DFT) used in this work, just like the other reactivity descriptors. According to the B3LYP level results, **CII** has the highest energy gap value, which means that it has the highest kinetic stability and less chemical reactivity. On the other hand, **CII** is the hardest conformer according to the global hardness value obtained by using the B3LYP level; the global hardness has changed as **CIII** (2.4829 eV) < **CIV** (2.4854 eV) < **CV** (2.5692 eV) < **CI** (2.6409 eV) < **CII** (2.6497 eV) in the chloroform phase and is almost similar to that of the gas phase. As it has been pointed out by Zhou and Parr,[30] the energy gap value order of the stable conformers is the same as the order of the hardness values. Also, we can easily say that all conformers are polarizable because of having a lower energy gap value than the urea ($\Delta E = 6.7063$ eV),[31] and this also supports the NLO results. From Table 3, the electrophilicity index orders of all stable conformers have been calculated as follows: **CIII** (2.0810 eV) < **CIV** (2.0818 eV) < **CI** (2.1706 eV) < **CII** (2.1785 eV) < **CV** (2.2543 eV) by the B3LYP level and **CIV** (3.0015 eV) < **CI** (3.0065 eV) < **CIII** (3.0089 eV) < **CII** (3.0097 eV) < **CV** (3.0104 eV) by the HF method. In any case, **CV** has the highest electrophilicity index, while **CIII** has the lowest electrophilicity index by the B3LYP level.

The HOMO and LUMO amplitudes for all conformers are given in Figure 3; the HOMO and LUMO amplitudes for the M06-2X level of the theory and the HF method are given in Supplemental Figure S1. It can be noted from Figure 3 that the HOMO density for **CIII** and **CIV** is mainly localized on R**C** and R**D** for both methods, which indicates that these conformers as nucleophiles will attack an external molecular site with the electrons localized on R**C** and R**D**. However, the HOMO for the **CII** is mostly located over the rings except for R**C**, and the acetyl group is attached to the N13 atom of the compound. However, the

Table 3. The calculated quantum chemical and physicochemical parameters of the five stable conformers of demethoxyaspidospermine in the chloroform phase.

	CI	CII	CIII	CIV	CV
B3LYP/6-311++G(d, p)					
HOMO (-*I*)	−0.2215	−0.2222	−0.2094	−0.2096	−0.2195
LUMO (-*A*)	−0.0274	−0.0275	−0.0269	−0.0269	−0.0307
Δ*E* (energy gap)	5.2817	5.2994	4.9658	4.9707	5.1383
χ	−3.3859	−3.3978	−3.2146	−3.2168	−3.4035
η	2.6409	2.6497	2.4829	2.4854	2.5692
ω	2.1706	2.1785	2.0810	2.0818	2.2543
ΔN_{max}	1.2821	1.2823	1.2947	1.2943	1.3247
M06-2X/6-311++G(d, p)					
HOMO (-*I*)	−0.2695	−0.2698	−0.2683	−0.2683	−0.2704
LUMO (-*A*)	−0.0057	−0.0053	−0.0058	−0.0061	−0.0054
Δ*E* (energy gap)	7.1778	7.1961	7.1435	7.1332	7.2094
X	−3.7448	−3.7431	−3.7291	−3.7331	−3.7525
H	3.5889	3.5980	3.5718	3.5666	3.6047
Ω	1.9538	1.9470	1.9466	1.9537	1.9531
ΔN_{max}	1.0434	1.0403	1.0440	1.0467	1.0410
HF/6-311++G(d, p)					
HOMO (-*I*)	−0.3033	−0.3033	−0.3036	−0.3036	−0.3053
LUMO (-*A*)	−0.0387	−0.0388	−0.0387	−0.0385	−0.0384
Δ*E* (energy gap)	7.1990	7.1974	7.2094	7.2137	7.2635
χ	−4.6523	−4.6542	−4.6575	−4.6531	−4.6761
η	3.5995	3.5987	3.6047	3.6069	3.6318
ω	3.0065	3.0097	3.0089	3.0015	3.0104
ΔN_{max}	1.2925	1.2933	1.2921	1.2901	1.2876

HOMO: highest molecular orbital; LUMO: lowest unoccupied orbital.
Δ*E* (energy gap), χ, η, ω, and ΔN_{max} are in electronvolt; HOMO and LUMO energies are in atomic units.

LUMO for all stable structures is mainly localized on R**A**, R**B**, and partly on R**E** for both methods, which means that all conformers will accept electrons from the outer molecular system to R**A**, R**B**, and R**E**.

MEP diagrams are used to predict the chemical reactivity tendency and intermolecular or intramolecular interactions that occur in a specific molecular system. MEP diagrams are represented by a color scheme expressing the electrostatic potential change with respect to the order: red (electron-rich region) < orange < yellow < green < light blue < blue (electron-poor region). Figure 3 also shows the MEP graphs for all conformers by the B3LYP level in the chloroform phase; the MEP diagrams for the M06-2X level of theory and the HF method have been given as Supporting Information in Supplemental Figure S1. Accordingly, the electron density for all conformers from the red to blue have changed as **CV** ($\pm 9.296e^{-2}$) < **CI** ($\pm 9.216e^{-2}$) < **CII** ($\pm 9.135e^{-2}$) < **CIV** ($\pm 9.132e^{-2}$) < **CIII** ($\pm 9.114e^{-2}$) by the B3LYP level and **CV** ($\pm 9.080e^{-2}$) < **CII** ($\pm 9.066e^{-2}$) < **CI** ($\pm 9.040e^{-2}$) < **CIV** ($\pm 9.027e^{-2}$) < **CIII** ($\pm 9.013e^{-2}$) by the HF method (Supplemental Figure S1). Accordingly, it can be said that **CV** and **CI** are more favorable for nucleophilic attack reactions than the other conformers because they have highly negative electrostatic potential values for their electron density surface. It is clear from Figure 3 that the acetyl group and aromatic R**A** having a red color shows the electron-rich region for all conformers for the nucleophilic attack. Moreover, the medium orange color for **CI**, **CII**, and **CV** appears around the N26 atom (at the conjunction point of R**D** and R**E**). On the other hand, the light blue color shows as an indicator that the electron-poor region for all conformers has been mainly calculated around the aliphatic rings as well as the ethyl group attached to the C15 atom at the conjunction point of R**C** and R**D**.

Vibrational analysis

The selected vibrational modes of the title compound are given in Supplemental Table S6; the simulated frequencies for the compound have been scaled down by using the scaling factor 0.960[32] for B3LYP/6-311++G(d, p), 0.9489[33] for M06-2X/6-311++G(d, p), and 0.9050[34] for HF, in order to make the calculated results compatible with the experimental results. Full potential energy distribution (PED) assignments and the vibrational frequencies of the most stable conformer can be seen from Supplemental Table S6. Figure 4 shows the observed and simulated infrared (IR) spectra. Also, the simulated IR spectra of each stable conformer have been given in Supplemental Figure S2.

Recently, the C=O vibration[35] was recorded by FTIR spectroscopy at 1725 and 1654 cm^{-1} and simulated by the B3LYP/6-311++G(d, p) level in the range 1789–1654 cm^{-1}.[35,36] Here, the C=O stretching signal occurred at 1672 cm^{-1} and simulated for the most stable conformer at 1623 (B3LYP), 1653 (M06-2X), and 1672 cm^{-1} (HF).

In the past, the aromatic C-C stretching modes for the imine oxime derivative were recorded at 1582 and 1579 cm^{-1} and simulated by the B3LYP/6-311++G(d, p)

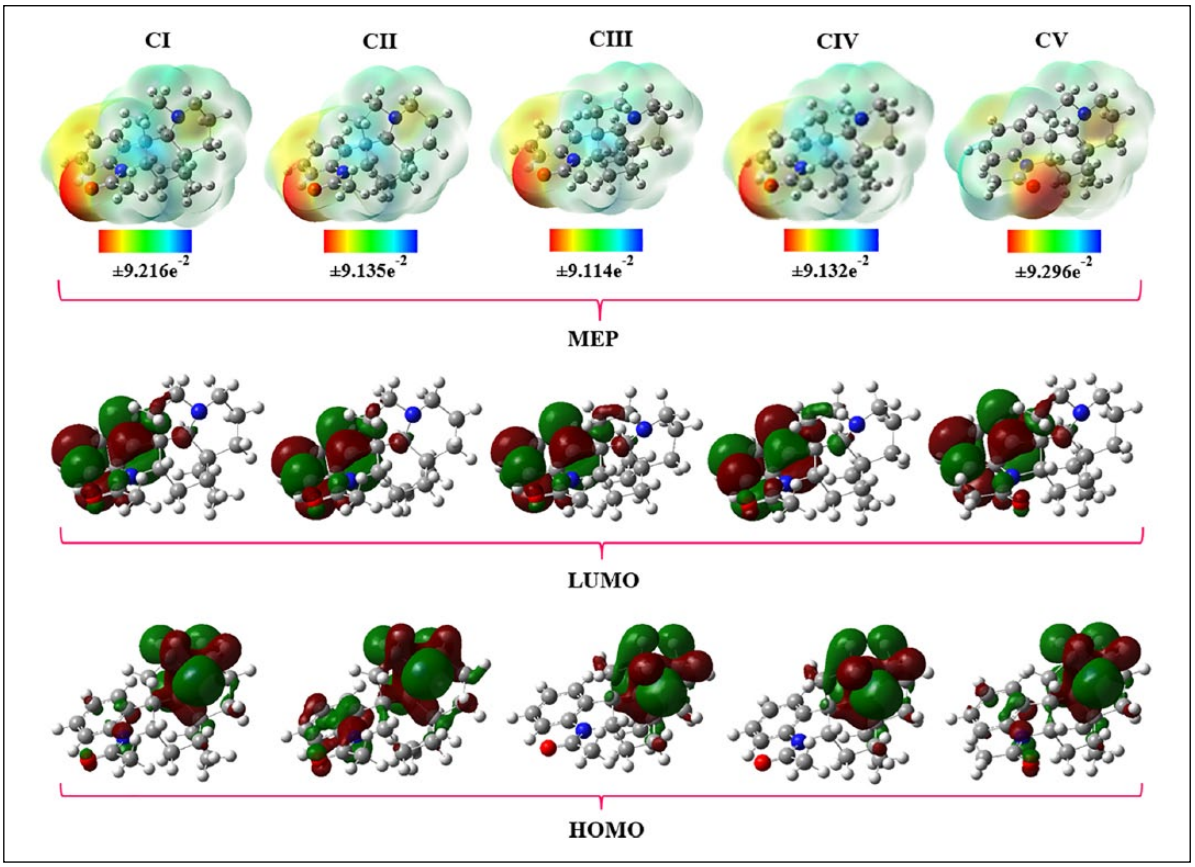

Figure 3. HOMO, LUMO (iso value: 0.02), and MEP (iso value: 0.0004) pilots of the five stable conformers for the demethoxyaspidospermine by using the B3LYP/6-311++G(d, p) level of the theory in the chloroform phase.

level at 1594 and 1577 cm^{-1}.[37] Also, Kanaani et al.[38] recorded the aromatic C-H stretching signals for the phenyl rings of a heterocyclic imidazole compound in the range 3182–2929 cm^{-1} by FTIR spectroscopy and simulated them in the range 3048–3086 cm^{-1} by the B3LYP/6-311++G(d, p) level of the theory. Moreover, they[38] observed in-the-plane (IPB) and out-of-the-plane (OPB) HCC bending modes in the range of 1334–1012 cm^{-1} and 926–560 cm^{-1}, respectively. Also, these bending modes for the imine oximes were calculated[37] in the range 1470–1040 cm^{-1} and 963–511 cm^{-1} by the B3LYP/6-311++G(d, p) level, respectively. Moreover, the symmetric CH_3 (νCH_3) and asymmetric CH_3 ($\nu_{as}CH_3$) stretching modes for the heterocyclic imidazole derivatives were calculated by DFT at 3031–3015 cm^{-1} and 2944 cm^{-1} and were recorded at 2895 and 2845 cm^{-1} in the IR spectrum, respectively.[38]

In this work, we have observed the C-C stretching bands for the aromatic part of the title compound at 1647 and 1594 cm^{-1} and simulated them at 1576, 1572, and 1011 cm^{-1} by the B3LYP level, whereas this mode has been assigned as 1592, 1583, and 1009 cm^{-1} by the M06-2X level and 1610, 1601, and 1005 cm^{-1} by the HF method. Also, the C-C stretching modes contaminated with the in-plane C-H bending (IPB HCC) modes have been calculated at 1453, 1436, 1259, 1141, 1075, and 1015 cm^{-1} by the B3LYP level and recorded at 1461 cm^{-1}. It can also be seen from Supplemental Table S6 that the other IPB HCC bending vibrational modes for the aromatic ring (R**A**) mixed with the twisting modes has been simulated at 1266 and 1133 cm^{-1} by the B3LYP level. On the other hand, the IPB HCC R**A** mode has been assigned in the range 1449–1070 cm^{-1} by the M06-2X level and in the range 1482–1085 cm^{-1} by the HF method. Also, the OPB HCC R**A** has been assigned as not mixed with the other modes by the B3LYP level at 963 (86%), 929 (73%), 852 (31%), and 740 cm^{-1} (78%) and simulated as a mixed mode at 863 (14%), 856 (40%), 750 (61%), 550 (36%), and 525 cm^{-1} (21%).

Here, the asymmetric and symmetric stretching modes for the methylene group ($\nu C_{39}H2$) have been calculated at 2948 (78%) and 2920 cm^{-1} (79%) by the B3LYP level, 2919 (91%) and 2885 cm^{-1} (85%) by the M06-2X level, and 2895 (67%) and 2861 cm^{-1} (74%) by the HF method. In addition, the symmetric stretching mode for the C_{40}-H3 and C_{49}-H3 groups of the title compound have been simulated by the B3LYP level at 2926 (83%)–2927 cm^{-1} (84%) and 2944 cm^{-1} (85%), respectively. Moreover, the symmetric bending vibration for the methyl groups has been assigned at 1370 and 1362 cm^{-1} for the C_{40}-H3 group and 1373, 1346, 1343, 1340, and 1336 cm^{-1} for the C_{49}-H3 group, at the B3LYP level. From Supplemental Table S6, the bending modes for the non-aromatic rings (R**C**, R**D**, R**E**) have been calculated by B3LYP as follows: σCH (scissoring) bending modes are in the range 1469–1429 cm^{-1}, the ωCH (wagging) modes are at 1370–1238 cm^{-1}, the τCH (twisting) modes are at 1323–896 cm^{-1}, and the ρCH (rocking) modes are at 1110–700 cm^{-1}.

The C-N stretching modes have generally appeared in the region of the IR spectra containing the mixed

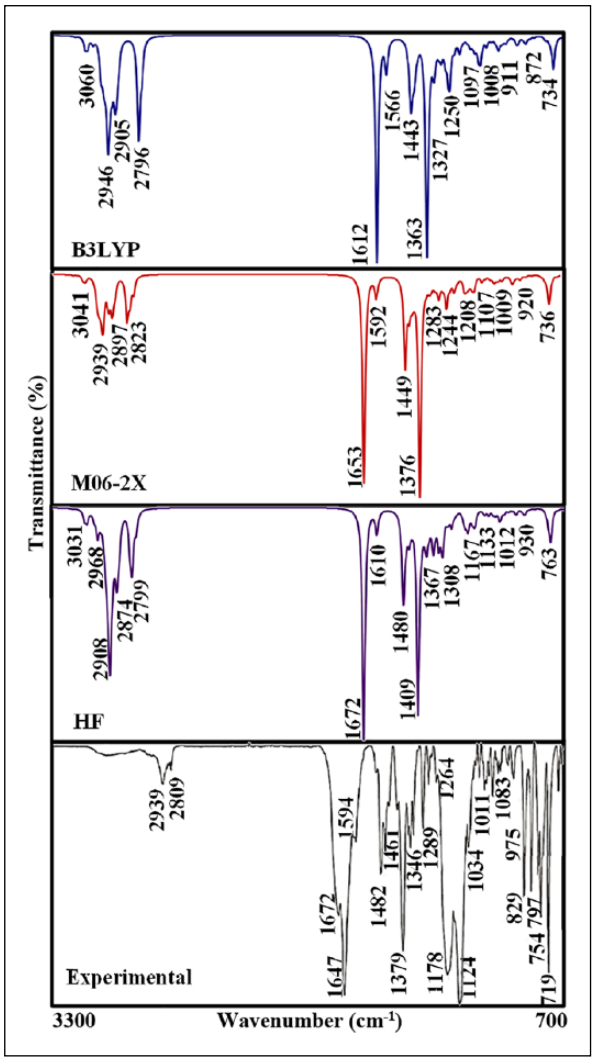

Figure 4. Experimental by FTIR and simulated IR spectra of demethoxyaspidospermine in the chloroform phase.

vibrational modes.[19,27,39] Recently, the νNC stretching modes were observed at 1594, 1341, 942, and 875 cm^{-1} by FTIR spectroscopy and at 1602, 1345, and 937 cm^{-1} by FT-Raman spectroscopy, also calculated[27] at 1596, 1343, 960, and 868 cm^{-1} by the B3LYP level. In this work, the νN13-C stretching modes for CI have been calculated by the B3LYP level at 1453, 1373, 1146, 1105, and 917 cm^{-1}, whereas the νN_{26}-C vibrations have been simulated at 1157, 1146, 1133, 1116, 1098, and 877 cm^{-1} (as not mixed). In addition, the νN_{13}-C and νN_{26}-C modes have given signals in the IR spectrum at 1461, and 1379, 903 and, 1124 and 878 cm^{-1}, respectively.

^{13}C and ^{1}H NMR spectral analyses

All computed data, including the B3LYP and M06-2X levels of the DFT method and HF method, can be seen in Supplemental Table S7a–7c. Also, the regression graphics and the correlation equations to show the agreement between the observed and simulated ^{1}H and ^{13}C NMR shifts have been given in Supplemental Figure S3 and Supplemental Table S8. Also, the observed ^{1}H and ^{13}C NMR spectra of the title compound are given in Supplemental Figure S4.

From Supplemental Table S8, the recorded chemical shifts are more compatible with those calculated by the DFT method than the HF method. In this work, the best correlation between the experimental and simulated ^{13}C NMR shifts were found for **CIV** (R^2 = 0.9986) by the B3LYP level and the **CI** (R^2 = 0.9955) by the HF method, in the chloroform phase. Furthermore, the best correlation between the observed and simulated ^{1}H shifts was found to be **CI** for all methods. Here, it can be concluded that the observed chemical shifts of the title compound agree with the simulated values because the correlation coefficient for each conformer is very close to 1.

In the past, ^{13}C NMR chemical shifts for the aromatic rings were observed in the range 116.3–150.1 ppm in $CDCl_3$ and simulated by the MPW1PW91 level in the range of 114.76–148.22 ppm in the gas phase.[40] In literature, non-aromatic ring ^{13}C isotropic chemical shifts for the dithiocarbamate derivatives were observed by Arslan et al.[41] in the range 25.0–47.90 ppm in DMSO and also predicted at 25.95–55.67 ppm by the B3LYP level. From Supplemental Table S7, the NMR signal for the C47 atom attached to the O48 atom has significantly shifted to high frequency; the ^{13}C chemical shift for the C47 atom has been recorded at 169.2 ppm and calculated at 175.9 ppm (**CI**) by the B3LYP level in the chloroform phase. As it is well known, the NMR chemical shifts strongly depend on the chemical environment of the related atoms;[42–44] the closer the atoms are to electronegative atoms, the higher the chemical shift values. Accordingly, the chemical shifts for the carbon atoms neighboring the N13 and N26 atoms have been observed at 53.5 (C7), 71.0 (C8), 67.0 (C14), 52.3 (C19), and 53.1 (C27) ppm, while the corresponding shifts for **CI** have been simulated by the B3LYP level of the theory at 60.1 (C7), 80.4 (C8), 77.3 (C14), 56.3 (C19), and 59.5 (C27) ppm. From Tables S7a–7c, the aromatic ring ^{13}C isotropic chemical shifts of the title compound have been observed in the range 119.1–142.0 ppm and have been calculated by the B3LYP level in the range 124.5–150.2 ppm (**CI**) and 121.4–152.9 ppm (**CV**), while these chemical shifts have been predicted by the HF method in the range 125.2–150.0 ppm for **CI** and 121.7–151.1 ppm for **CV**, in the chloroform phase.

In recent work, the ^{1}H NMR chemical shifts of the aromatic ring for a carbazole derivative were observed[43] in the range 7.24–7.78 ppm and simulated by the DFT method at 6.35–7.76 ppm, whereas the non-aromatic shifts were recorded at 1.78–2.94 ppm and calculated at 1.99–3.21 ppm. In this study, the aromatic ring proton signals for the studied compound have been observed at 6.97–8.51 ppm. In addition, the simulated signals are in the range of 7.31–8.47 ppm for **CI** and in the range of 7.30–8.43 ppm for **CIV** by B3LYP (chloroform phase), while the corresponding signals for **CI** and **CIV** have been computed by M06-2X in the range 7.94–9.00 ppm and 7.93–8.96 ppm, respectively. Moreover, it can be seen from Supplemental Table S7 that the NMR shifts computed by M06-2X are higher than the corresponding ones calculated by the B3LYP level as well as by the HF method. Also, the proton NMR signals for the H20, H30, and H46 atoms neighboring the nitrogen atom have been observed at 3.03, 2.99, and 3.80 ppm,

respectively, whereas the same shifts for **CI** have been computed by the B3LYP level (chloroform phase) at 3.23, 3.08, and 3.91 ppm. As expected, the ^{1}H NMR shifts for the ethyl group atoms of **CI** have been observed in the range 0.57–0.86 ppm and simulated by the B3LYP level (chloroform phase) in the range of 0.56–1.28 ppm.

Conclusion

In this paper, we have highlighted the importance of investigation of Aspidosperma-type alkaloids, considering their widespread application in the traditional medicine and their vast array of potential biomedical applications. We then demonstrated a one-step method for synthesizing demethoxyaspidospermine, which is well known as an Aspidosperma-type alkaloid. The development of synthetic organic chemistry approaches to obtain these substances can make their future extraction from natural sources unnecessary.

In addition, the conformational analysis has revealed the five stable structures, the relative free energies of which have changed from 0.0 to 3.34 kcal mol^{-1} by using the B3LYP level in chloroform. NBO analysis has shown that the resonance interactions ($\pi \rightarrow \pi^*$) have been mainly responsible for the stabilization energy lowering for all stable conformers, but also the hyperconjugative interactions ($\sigma \rightarrow \pi^*$) for **CI**, **CII**, and **CV** have partly contributed to the lowering of the stabilization energy. HOMO and LUMO density and MEP diagrams have been used to show the reactive sites of each stable conformer. According to the NLO analysis results, all conformers have contributed to the optical behavior of the compound because their β tensors have been calculated to be higher than those of urea.

Experimental

Reagents to synthesize of the title compound were purchased from Sigma and used as received. The reaction was monitored by thin-layer chromatography (silica gel 60 F254), and the melting point of the compound was determined using a capillary tube on a GallenKamp apparatus and uncorrected. ^{1}H NMR (400 MHz) and ^{13}C NMR (100 MHz) spectra were recorded in $CDCl_3$ mixed with DMSO on a Bruker instrument DPX-400 MHz (high-performance digital FT–NMR spectrometer). The recorded chemical shifts are referenced to tetramethylsilane (TMS), and the δ coupling values are expressed in per million (ppm) and in Hertz (Hz), respectively. The FTIR spectrum of the title compound was recorded using a Mattson 1000 FTIR spectrometer using the KBr pellet method between 4000 and 400 cm^{-1} wave numbers (128 scans to get 4.0-cm^{-1} resolution). The mass spectrum was obtained using an Agilent 5973 gas chromatograph-mass spectrometer (GC-MS). A Costech ECS 4010 analyzer was used to perform the elemental analyses.

Synthesis of (+)-demethoxyaspidospermine **(2)**. A mixture of aspidospermidine (**1**) (50 mg, 0.17 mmol), and tetrabutylammonium hydrogensulfate (120.19 mg, 0.354 mmol) and sodium hydroxide (30 mL, 25%) in dichloromethane (30 mL) was cooled in an ice bath under a nitrogen atmosphere for 2 h. Next, acetic anhydride (0.71 mmol, 0.8 mL) was added dropwise, and the mixture stirred for 6 h at room temperature. Upon completion of the reaction (monitored by thin-layer chromatography (TLC)), the phases were separated by adding water (30 mL). The organic layer was dried over Na_2SO_4, and the solvent was evaporated. The residue was purified by silica gel chromatography using diethyl ether–ethyl acetate (4:1) to give 46.52 mg of demethoxyaspidospermine **(2)** as a brown oil in milligram, (81% yield). IR spectrum (ν, cm^{-1}): 3030 (aromatic C–H), 2939 (=C–H), 2689 (C–H), 1672 (C=O), 1647 (C=C), 1594, 1482, 1461, 1379, 1178, 1124, 719. ^{1}H NMR (400 MHz, $CDCl_3$): δ 0.57 (3H, t, J = 7.3 Hz), 0.80 (1H, dq, J = 14.3, 7.3 Hz), 0.86 (1H, d, J = 13.4 Hz), 1.08 (1H, dd, J = 13.4, 4.3 Hz), 1.12–1.18 (1H, m), 1.40 (2H, dd, J = 14.3, 3.4 Hz), 1.44–1.51 (1H, m), 1.54–1.58 (2H, m), 1.60–1.69 (1H, m), 1.92–1.98 (2H, m), 2.02 (1H, dd, J = 13.3, 4.0 Hz), 2.19 (3H, s), 2.23 (1H, s), 2.24–2.33 (1H, m), 2.92–2.99 (1H, m), 3.03 (1H, dt, J = 8.7, 2.5 Hz), 3.80 (1H, dd, J = 11.3, 6.3 Hz), 6.97 (1H, t, J = 7.4 Hz), 7.15–7.24 (2H, m), 8.51(1H, d, J = 7.8 Hz). ^{13}C NMR (100 MHz, $CDCl_3$): δ 7.2, 21.2, 23.0, 23.7, 26.1, 30.5, 33.9, 36.6, 39.1, 52.3, 53.1, 53.5, 67.0, 71.0, 119.1, 123.4, 125.1, 128.8, 138.2, 142.0, 169.2. Found, %: C, 77.68; H, 8.63; N, 8.71. $C_{21}H_{28}N_{2O}$. Calculated, %: C, 77.74; H, 8.70; N, 8.63.

Computational details

The stable conformational structures of demethoxyaspidospermine were determined with the PES scan analysis by using the B3LYP/6-31G(d, p) level of the theory[45,46] in the gas phase. Then, the five stable conformers obtained from the conformational analysis scan were re-optimized with 6-311++G(d, p) basis set by using the B3LYP and M06-2X[47] levels and HF method. The second-order perturbation analysis in the NBO (NBO basis)[24,25] was employed to search the intramolecular charge transfer between the donor and acceptor orbitals, being important in terms of the biological or pharmaceutical importance of each stable conformer. In addition, the optical properties of each stable conformer were determined with NLO analysis. The Gauge-Independent Atomic Orbital (GIAO)[48,49] approach was used to predict the ^{1}H and ^{1}C NMR chemical shifts of each stable conformer of demethoxyaspidospermine by subtracting the shielding constants of TMS. The polarized continuum model (PCM)[50,51] was used to simulate the chloroform environment. All calculations of the title compound were conducted with Gaussian 09W.[52] GaussView 6.0[53] was used to verify the vibrational modes of the title compound as well as to give the pictorial representations of the FMO and MEP diagrams. The VEDA package[54] was used to assign the vibrational frequencies of the title compound via the PED analysis.

By Koopmans' theorem for the HF method and by Janak's theorem for DFT functionals, the ionization energy (I) and electron affinity (A) based on the FMO energies have been calculated with the equations (1) and (2).[55,56] Also, the global reactivity descriptors, including

the electronic chemical potential (χ), global hardness (η), electrophilicity (ω), and the maximum charge transfer index (ΔN_{max}),[57–59] are given in equations (3)–(6)

$$I = -E_{\mathrm{HOMO}} \tag{1}$$

$$A = -E_{\mathrm{LUMO}} \tag{2}$$

$$\chi = -\frac{I + A}{2} \tag{3}$$

$$\eta = \frac{I - A}{2} \tag{4}$$

$$\omega = \frac{\mu^2}{2\eta} \tag{5}$$

$$\Delta N_{max} = \frac{I + A}{2(I - A)} \tag{6}$$

The static dipole moment (μ), the mean polarizability (α_0), the anisotropy of the polarizability ($\Delta\alpha$), and the frequency-independent first-order hyperpolarizability (β) tensors used in predicting the NLO properties of the title compound were calculated from the equations given below[60,61]

$$\mu = \left(\mu_x^2 + \mu_y^2 + \mu_z^2\right)^{\frac{1}{2}} \tag{7}$$

$$\alpha_0 = \frac{\left(\alpha_{xx} + \alpha_{yy} + \alpha_{zz}\right)}{3} \tag{8}$$

$$\Delta\alpha = 2^{-\frac{1}{2}}\left[\begin{array}{l}\left(\alpha_{xx} - \alpha_{yy}\right)^2 + \left(\alpha_{yy} - \alpha_{zz}\right)^2 \\ +\left(\alpha_{zz} - \alpha_{xx}\right)^2 + 6\left(\alpha_{xz}^2 + \alpha_{xy}^2 + \alpha_{yz}^2\right)\end{array}\right]^{\frac{1}{2}} \tag{9}$$

$$\beta = \left(\beta_x^2 + \beta_y^2 + \beta_z^2\right)^{\frac{1}{2}} \tag{10}$$

where

$$\beta_x = \left(\beta_{xxx} + \beta_{xyy} + \beta_{xzz}\right) \tag{11}$$

$$\beta_y = \left(\beta_{yyy} + \beta_{yzz} + \beta_{yxx}\right) \tag{12}$$

$$\beta_z = \left(\beta_{zzz} + \beta_{zyy} + \beta_{zxx}\right) \tag{13}$$

Declaration of conflicting interests

The author(s) declared no potential conflicts of interest with respect to the research, authorship, and/or publication of this article.

Funding

The author(s) disclosed receipt of the following financial support for the research, authorship, and/or publication of this article: This work was supported by the Scientific and Technological Research Council of Turkey (TUBITAK, Project No. 112T503) and Sivas Cumhuriyet University, Scientific Research Projects Department (Grant number: CUBAP: EĞT-072). All calculations were carried out at TUBITAK ULAKBIM, High Performance, and Grid Computing Center (TR-Grid e-Infrastructure).

ORCID iDs

Goncagül Serdaroğlu https://orcid.org/0000-0001-7649-9168

Nesimi Uludağ https://orcid.org/0000-0002-2819-3612

Supplemental material

Supplemental material for this article is available online.

References

1. Coppen JJW and Cobb AL. *Phytochemistry* 1983; 22: 125.
2. Nogueira PCN, Araújo RM, Viana GSB, et al. *J Braz Chem Soc* 2014; 25: 2108.
3. Guimarães HA, Braz-Filho R and Vieira IJR. *Molecules* 1983; 17: 3025.
4. Deutsch HF, Evenson MA, Drescher P, et al. *J Pharm Biomed Anal* 1994; 12: 1283.
5. Maes D and Maes R. *Rev Bras Farmacogn* 2015; 25: 42.
6. Marino JP, Rubio MB, Cao G, et al. *J Am Chem Soc* 2002; 124: 13398.
7. Nidhiry JE and Prasad KR. *Tetrahedron* 2013; 69: 5525.
8. Kozmin SA and Rawal VH. *J Am Chem Soc* 1998; 120: 13523.
9. Callaghan O, Lampard C, Kennedy AR, et al. *J Chem Soc Perkin Trans 1* 1999; 8: 995.
10. Stork G and Dolfini JE. *J Am Chem Soc* 1963; 85: 2872.
11. Node M, Nagasawa H and Fugi K. *J Org Chem* 1990; 55: 517.
12. Gallagher T, Magnus P and Huffman J. *J Am Chem Soc* 1982; 104: 1140.
13. Laronze J-Y, Laronze-Fontaine J, Levy J, et al. *Tetrahedron Lett* 1974; 15: 491.
14. Patir S and Uludag N. *Tetrahedron* 2009; 65: 115.
15. Uludag N and Yakup M. *Org Prep Proced Int* 2015; 47: 454.
16. Uludag N, Yilmaz R, Asutay O, et al. *Chem Heterocycl Compd* 2016; 52: 196.
17. Uludag N, Uyar T and Patir S. *Org Prep Proced Int* 2003; 35: 397.
18. Uludag N and Serdaroglu G. *J Mol Struct* 2018; 1155: 548.
19. Uludag N, Serdaroglu G and Yinanc A. *J Mol Struct* 2018; 1161: 152.
20. Serdaroglu G and Uludag N. *J Mol Struct* 2018; 1166: 286.
21. França OO, Brown RT and Santos CAM. *Fitoterapia* 2000; 71: 208.
22. Hökelek T, Şahin E, Uludag N, et al. *Acta Crystallogr* 2008; E63: o3268.
23. Murugavel S, Kannan PS, SubbiahPandi A, et al. *Acta Crystallogr* 2008; E64: o2433.
24. Weinhold F, Landis CR and Glendening ED. *Int Rev Phys Chem* 2016; 35: 399.
25. Reed AE, Curtiss LA and Weinhold F. *Chem Rev* 1988; 88: 899.
26. Rajeshirke M and Sekar N. *Opt Mater* 2018; 76: 191.
27. Raja M, Muhamed R, Muthu S, et al. *J Mol Struct* 2017; 1141: 284.
28. Aihara J. *Theor Chem Acc* 1999; 102: 134.

29. Aihara J. *J Phys Chem A* 1999; 103: 7487.
30. Zhou Z and Parr RG. *J Am Chem Soc* 1990; 112: 5720.
31. Soliman SM, Hagar M, Ibid F, et al. *Spectrochim Acta A* 2015; 145: 270.
32. Shakila G, Saleem H and Sundaraganesan N. *World Sci News* 2017; 61: 150.
33. Sert Y, Balakit AA, Öztürk N, et al. *Spectrochim Acta A* 2014; 131: 502.
34. Karabacak M, Coruh A and Kurt M. *J Mol Struct* 2008; 892: 125.
35. Hasan T, Mehdi SH, Ghalib RM, et al. *J Chem Sci* 2015; 127: 2217.
36. Sayin K and Üngördü A. *Spectrochim Acta A* 2018; 193: 147.
37. Kaya Y. *J Chem Sci* 2016; 128: 1479.
38. Kanaani A, Ajloo D, Kiyani H, et al. *J Chem Sci* 2016; 128: 1211.
39. Yadav MPS, Kumar A and Jayarama A. *Monatsh Chem* 2016; 147: 1045.
40. John NL, Joy LK, Kumar MS, et al. *Mol Simulat* 2018; 44: 40.
41. Arslan NB, Kazak C and Aydın F. *J Mol Struct* 2018; 1155: 646.
42. Serdaroglu G and Uludag N. *Bulg Chem Commun* 2018; 50: 25.
43. Serdaroğlu G and Şahin N. *J Mol Struct* 2019; 1178: 212.
44. Agarwal P, Choudhary N, Gupta A, et al. *Vib Spectrosc* 2013; 64: 134.
45. Becke AD. *J Chem Phys* 1993; 98: 1372.
46. Lee C, Yang W and Parr RG. *Phys Rev B* 1988; 37: 785.
47. Zhao Y and Truhlar DG. *Theor Chem Acc* 2008; 120: 215.
48. Rohlfing CM, Allen LC and Ditchfield R. *Chem Phys* 1984; 87: 9.
49. Wolinski K, Hinton JF and Pulay P. *J Am Chem Soc* 1990; 112: 8251.
50. Foresman JB, Keith TA, Wiberg KB, et al. *J Phys Chem* 1996; 100: 16098.
51. Tomasi J, Mennuci B and Cammi R. *Chem Rev* 2005; 105: 2999.
52. Frisch MJ, Trucks GW, Schlegel HB, et al. *Gaussian 09, revision D.01*. Wallingford, CT: Gaussian, Inc., 2016.
53. GaussView 6.0. Wallingford CT: Gaussian, Inc., 2016.
54. Jamroz MH. Vibrational energy distribution analysis, VEDA 4, Warsaw, 2004-2010.
55. Koopmans T. *Physica* 1934; 1: 104.
56. Janak JF. *Phys Rev B* 1978; 18: 7165.
57. Parr RG and Pearson RG. *J Am Chem Soc* 1983; 105: 7512.
58. Pearson RG. *Proc Natl Acad Sci USA* 1986; 83: 8440.
59. Parr RG, Szentpaly LV and Liu S. *J Am Chem Soc* 1999; 121: 1922.
60. Garza AJ, Osman OI, Asiri AM, et al. *J Phys Chem B* 2015; 119: 1202.
61. Adeniyi AA and Conradie J. *J Mol Model* 2019; 25: 78.